X-ray microtomography reveals the 3D enzymatic deconstruction pathway of raw lignocellulosic biomass

S Blosse, Antoine Bouchoux, C Y Montanier, Paul Duru

X-ray microtomography reveals the 3D enzymatic deconstruction pathway of raw lignocellulosic biomass

S. Blosse[1,2], A. Bouchoux[2], C.Y. Montanier[2]✉, P. Duru[1]✉

In the context of the development of a circular bioeconomy, plant biomass constitutes a vast potential source of renewable molecules of interest. The industrial process essentially consists in using enzymes for its deconstruction. However, we are still lacking a precise understanding of the enzymes' action on such a complex, multiscale porous material. Here, we demonstrate that X-ray microtomography tackles this question in a unique way, making it possible to follow precisely the enzymatic degradation of a model biomass, wheat straw. We perform a thorough analysis of the imaging results over the full length scale of the sample and as a function of degradation time. In particular, we observe the progressive disappearance of specific cellulose-rich cell walls, with distinct 3D heterogeneities in the enzymatic action at different times and length scales. Those 3D pieces of information about the degradation process contrast clearly with those obtained from classical 2D imaging techniques.

[1]Institut de Mécanique des Fluides de Toulouse (IMFT), Université de Toulouse, CNRS-Toulouse, Toulouse, France. [2]TBI, Université de Toulouse, CNRS, INRAE, INSA, Toulouse, France. ✉email: paul.duru@imft.fr (P. Duru), cedric.montanier@insa-toulouse.fr (C.Y. Montanier).

Keywords:

X-ray microtomography

3D imaging processing

Wheat straw

Plant cell wall

Enzymatic hydrolysis

Highlights:

3D imaging of wheat straw sample by X-ray µCT, before and after enzymatic hydrolysis

Enzymatic action imaged at different times and length scales

The enzymatic action concentrates on parenchyma cell walls

Extraction of markers for enzymatic degradation from 3D images

Highlighting of the 3D heterogeneities of the enzymatic attack

Graphical Abstract:

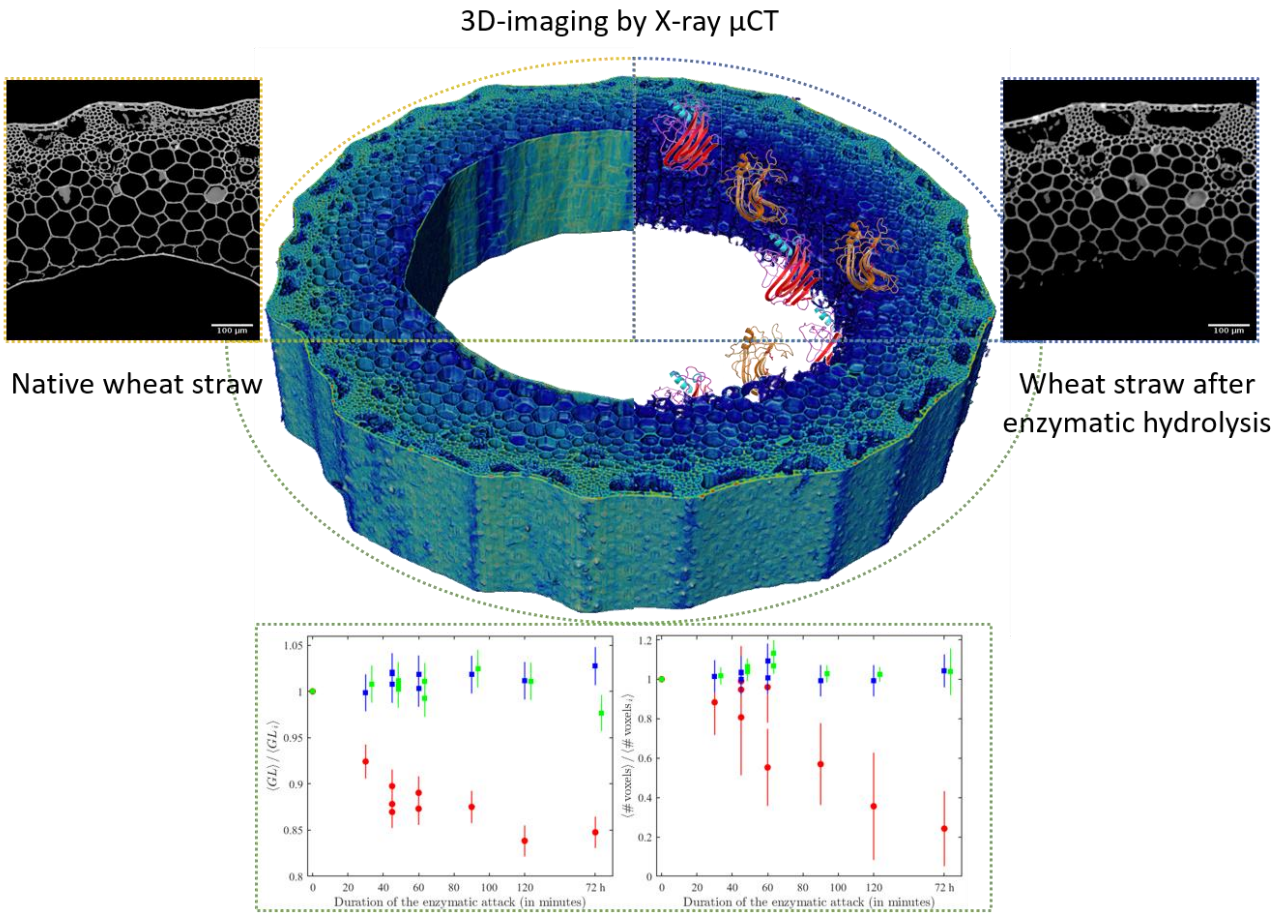

Markers quantifying enzymatic degradation from 3D image processing

1. Introduction

Lignocellulosic biomass, *i.e.*, the cell walls of plants (PCWs), is the largest reservoir of organic carbon on Earth. One huge source of PCW biomass is the by-products of agriculture, which can possibly be used for producing quantities of renewable and sustainable molecules and materials for our daily lives (Cherubini, 2010) For such a valorisation to be performed, lignocellulosic biomass must be decomposed into small elementary pieces, *i.e.*, (macro-)molecules or synthons. This 'deconstruction' process is, however, not an easy task as plants have constantly evolved for protecting themselves from external aggressions (Morris et al., 2018 ; Zhang et al. 2021). This led to PCWs having structures and compositions that are always very complex, even if they obviously vary from one species to another.

The average PCW consists in an intricate composite matrix of cellulose, hemicelluloses, proteins and lignin; all components being - covalently or not - linked to each other (Amos and Mohnen, 2019). As we just stressed, this material is highly recalcitrant to chemical or biological degradation. However, cellulolytic microorganisms such as bacteria and fungi also evolved on their side for being able to use the PCW biomass as carbon feedstock. In that case, the attack is performed by lignocellulolytic enzymes that are produced by the microorganisms (Lopes et al., 2018). The enzymes involved are mainly glycoside hydrolases (GHs), a large and diverse group of enzymes that hydrolyse the glycosidic linkages between carbohydrates. GHs include cellulases, hemicellulases and pectinases, as a function of their specificity for a given substrate (Gilbert, 2010).

Extensive research has been carried out in the past years with the aim of achieving the enzymatic deconstruction on an industrial scale and designing processes that are economically viable. Studies focus mainly on the research and design of better GHs and on the description of their enzymatic action at the molecular scale. For practical reasons, most of those works are performed using synthetic chromogenic substrates and/or purified polysaccharides (Liberato et al., 2016 ; Gilmore et al., 2020 ; Badruna et al., 2021) . However, this leads to a characterization of the enzymes in conditions that are far from the 'real-life' conditions where enzymes face a raw natural substrate. One first disadvantage of such an approach has to do with the specific recognition interactions that exist between the enzyme and its real substrate and that triggers the catalysis. When using artificial and/or isolated substrates, the conditions for this recognition are not satisfied which can lead to a wrong estimation/understanding of the enzymatic activity towards a real substrate (Montanier et al., 2009). The second downside has to do with the accessibility of the enzyme to its substrate, which is dramatically facilitated using purified polysaccharides as opposed to polysaccharides that are embedded in a PCW.

Of course, there have been attempts for tracking and following enzymes' action on a real, natural substrate. Those are mainly microscopy-based studies which, indeed, make it possible to visualize the enzymes and/or the degraded material in conditions that are very close to the real ones (Hervé et al., 2009 ; Zeng et al., 2016 ; Devaux et al., 2018 ; Zoghlami and Paës, 2019 ; Herbaut et al., 2018) . However, there are still some limitations in those works. The substrate, e.g., corn or tobacco, is often prepared as quasi-2D slices, making it greatly overexposed to the enzymatic attack as compared to the reality. Such 2D-limited approaches do not allow to tackle important questions related to the diffusion and propagation of the enzymes in the material that they degrade. Furthermore, while some microscopy techniques such as confocal microscopy may lead to 3D images of samples with minimal preparation, the true extent of the observation range along the optical axis is always limited, and typically smaller than the characteristic size of the structure in that direction (*e.g*. cell size). It is therefore not straightforward to conclude about the crucial question of the heterogeneity of the degradation in real conditions and at all relevant length scales in the three space directions.

Clearly, a major step in the understanding of the enzymatic degradation of PCW biomass would be to visualize the degradation of a raw, natural, material in its three dimensions and using a technique that is less invasive as possible. In this article, we demonstrate that X-ray Computed microTomography (µCT) is the technique of choice. µCT is a non-destructive technique that provides 3D images of a sample without any specific preparation, notably without cutting which would lead to exposure of some internal regions of the sample. Laboratory tomography devices (by opposition to synchrotron-based tomography) allow to analyse millimetre-sized samples with a resolution of ~1 μm^3 in voxel size (Withers, 2007), which is clearly compatible with the dimensions of the PCW features (Hervé et al., 2009). Therefore, µCT allows to image samples over the 3 directions of space, with a field of view larger than the extent of the typical biomass anatomical feature (the extent of the plant cell in the straw longitudinal direction can be larger than 100 µm). This is made possible because biomass is transparent to X-ray. Imaging using visible-light sources, such as those used in conventional or confocal microscopy, is typically limited by the limited penetration depth of the light. The literature reports the use of µCT for exploring plant and wood microstructures (Matsushima et al. 2013; Mathers et al., 2018; Jones et al. 2021; Trtik et al., 2007; Strullu-Derrien et al. 2014; Mayo et al., 2010; Brereton et al. 2015), measuring the swelling properties of wood (Derome et al., 2011), analysing the water content of individual plant cells (Suuronen et al., 2013; Torres-Ruiz et al., 2016), or even localizing mineral particles in sugar cane bagasse (Yancy-Caballero et al., 2017). However, and to the best of our knowledge, µCT has never been used for investigating the enzymatic deconstruction of a PCW biomass sample.

In the present work, wheat straw (WS) is used as a model of both lignocellulosic biomass and agricultural by-product. We first show µCT 3D images of the raw, native samples, *i.e.*, before any

degradation. The general structure of those control samples is briefly discussed, with an emphasis on some specific and little-known features that µCT is able to detect. We then present the µCT 3D images of WS samples that have been degraded using a commercial cocktail of lignocellulolytic enzymes at different times. We perform a careful analysis of these images using a procedure that increases in complexity with (i) a first qualitative human-driven analysis of the data, (ii) a computer-driven statistical analysis of the enzymatic degradation curse, (iii) a focus on the 3D heterogeneity of the attack as only µCT can characterize. Our results clearly demonstrate that µCT is particularly well-suited to reveal the modification of the PCWs within our sample at different stages of the enzymatic deconstruction and that its 3D character is of importance to take into account the complexity of the bioconversion.

2. Materials & Methods

Sample preparation

Samples consist in wheat straw (*Triticum aestivum*, cv. Apache, France) intermodal section of 1 cm height, approximately 2 mm diameter and 0.4 mm thickness, harvested in summer 2010 and dried on site. Before using any strands of wheat straw, samples were washed in three successive baths of deionised water for 5 minutes, 10 minutes and one hour, and then dried for 6 hours in a ventilated oven at 45°C.

Then, to degrade the wheat straw, a commercial enzymatic cocktail, Novozymes Cellic HTEC2 (VHN00003, Luna No. 2010-01668-01), was used at a loading amount of 120 µg of proteins (~500 µg of HTEC2 solution) per mg of wheat straw. This cocktail was favored in order to provide an enzymatic activity compatible with an observation of the early stages of the parenchyma cell walls deconstruction. The enzymatic reaction was performed at 45°C under constant agitation at 1000 rpm (ThermoMixer C, Eppendorf) in 2 mL centrifuge tube (1800 µl of a 50 mM citrate buffer at pH 5.4 supplemented with 0.1 mg/mL BSA and 200 µl of HTEC2 diluted 500 times), during a controlled amount of time (from 30 to 120 minutes). Finally, the samples were dried in a ventilated oven at 45°C for 6 hours.

The enzymatic activity of the cocktail was determined by dinitrosalicylic acid (DNSA) assays, performed on native samples, to estimate the concentration of reduction sugar equivalent to xylose (Appendix C). Samples were first scanned before enzymatic degradation and then after exposure to the enzymatic cocktail. Preliminary results have shown that exposing twice a given sample to an enzymatic digestion may lead to significant deformation of the sample, certainly provoked by the imbibition and drying

procedures involved in the protocol. This precludes the image analysis, which requires to be able to find and follow the same 3D locations in the sample before and after digestion. Consequently, we used multiple native samples, each being subjected to one single enzymatic attack of controlled duration.

X-ray micro-CT

Samples were 3D-scanned using a Phoenix Nanotom tomograph, at high spatial resolution, with an isotropic voxel size of 1.25 µm. The distance between the sample axis of rotation and the exit window of the X-ray source was 4 mm. The sample bottom part was partially inserted in a capillary tube with 2 mm inner diameter, held by a three-jaw chuck. The top part of the sample was directly exposed to the X-ray beam. Image acquisition was performed at a 45 kV voltage and 250 µA amperage, 1700 radiographies were taken with an exposure time of 1250 ms and 4 frames averaging for a total scanning time of around 3 hours. Correction of ring artefacts and reconstruction was performed using the Phoenix Datos|X software. The image analysis detailed in the present paper was performed over a 3D reconstructed volume of 1.25 mm in height, equivalent to 1000 transverse tomographic slices.

Image Processing

The reconstructed 3D volume of the sample was imported into the commercial software Avizo (ThermoFischer Scientific, Waltham, Ma, USA). The first stage of image processing was noise removal using the non-local mean filtering (NLMF) function implemented in Avizo. Filtered tomographic slices were then exported and further processed using Matlab, by performing basic operations over sets of regions of interests located within the 3D image. Volume rendering required a few supplementary steps using Avizo. Segmentation of the image (i.e. separation between the two constitutive materials -air and plant cell walls-) was made using a hysteresis thresholding algorithm and led to a binary image. To remove all the air background, we used the mask function that overlaps the binary image (the mask) and the original grey level (GL) image. Voxels belonging to both the mask and the GL image were retained, together with their GL values, the other being set to zero. Finally, the volume rendering tool was used to obtain the 3D-representation shown in this paper. The image processing workflow, details about the procedures and validation tests are given In Appendix A.

3. Results and Discussion

Native wheat straw

All the images showed in this article are obtained using a µCT Phoenix/GE Nanotom system following a protocol detailed in the Methods section. In Fig. 1, we give the results for one native wheat straw sample, i.e., before any enzymatic treatment. The figure is divided in sub-pictures that together provide a summary of our approach and its performance. Fig. 1a shows the 3D volume rendering of the sample as reconstructed from the µCT data. Details about the image processing steps are given in the Methods section. The voxel size is 1.25 μm^3, which is clearly in the high-resolution range of µCT (Jones et al., 2021; Mayo et al., 2010). The colours of the images correspond to different contrasts between the material and its environment (air). This contrast is roughly proportional to the electron density in the voxels which in turn is related to the average mass density for such biomass samples (Trtik et al., 2007). However, the technique does not allow to exactly quantify the mass density and the colour scale is in arbitrary units. The 3D image of Fig.1a therefore represents the semi-quantitative distribution of the mass density in the material.

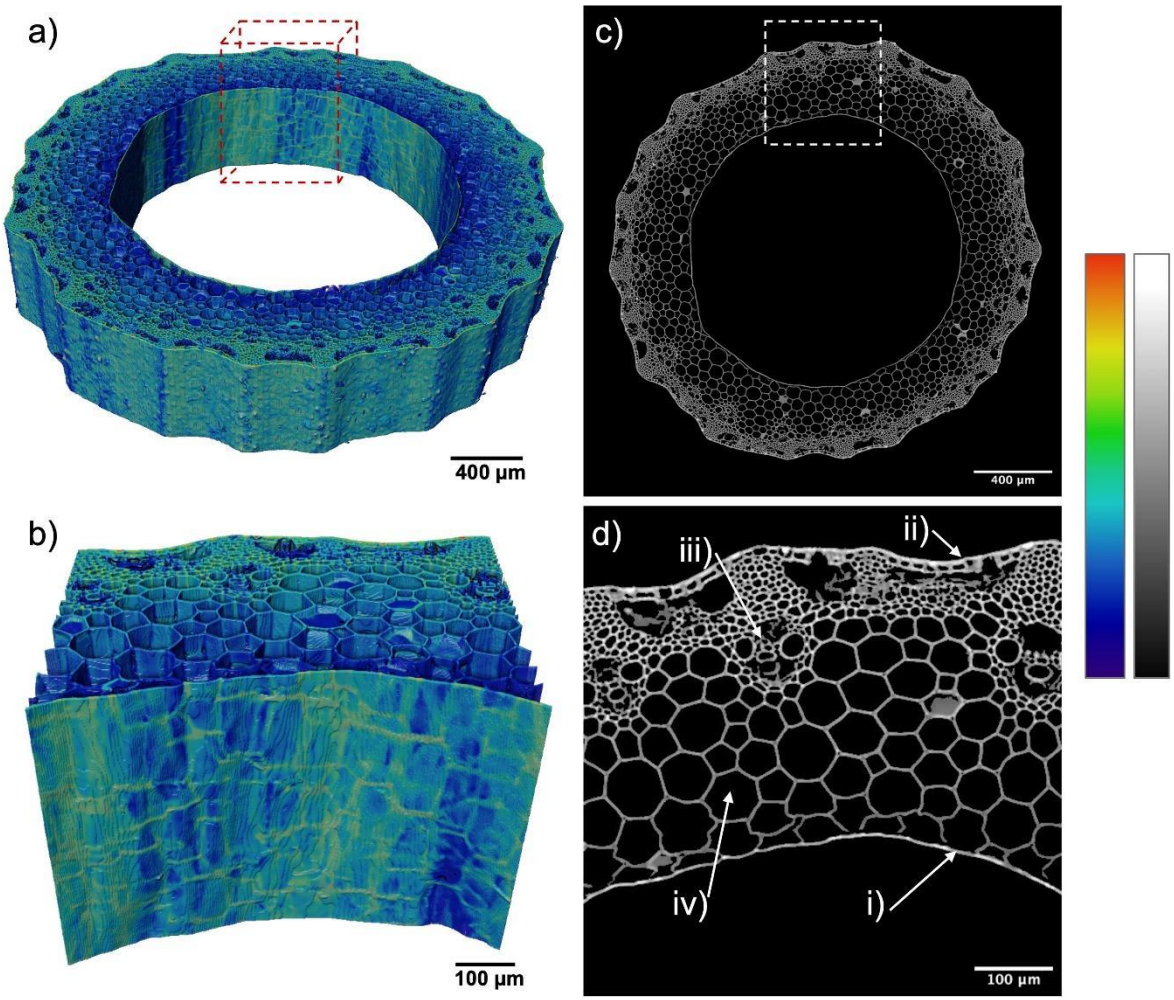

Fig. 1 µCT images of native wheat straw. a) 3D volume rendering (for sake of clarity, only one third of the full reconstructed volume is shown). b) 3D close-up (the front side in the inside wall of the straw, see the dashed red box in a). c) Tomographic transverse slice (taken in the middle of the 3D volume shown in a). d) Close-up of the transverse slice over the dashed white square shown in c). Several anatomical features are indicated: pith cavity lining -PCL- (i), epidermis (ii), large vascular bundles (iii), parenchyma cells (iv). The correspondence between the grey levels of the 2D images and the colormap of the 3D volumes is given on the right.

The straw has a tubular structure with an inner circular surface that appears smooth at the micron scale. The outer surface is more rugged and presents ~30-50 µm high corrugations that can be associated with a radial elementary pattern of the structure that repeats to form the ring. A 3D close-up that englobes this pattern is given in Fig. 1b. One less impressive but more convenient way to look at these results is to focus on a tomographic transverse slice of the sample (Fig. 1c and the corresponding close-up in Fig. 1d). To facilitate the visualization, such 2D images are given as grayscale images where black has the lowest mass density and white the highest. The main anatomical features of WS are clearly discernible on all these images, especially on Fig. 1d where they are annotated specifically. Different types of cells constitute the structure, with sizes ranging from ~70 µm next to the inner surface, to smaller cells of ~10 µm next to the outer surface. We will not go into a detailed description of the anatomy of WS here as it is already well documented (Nassar et al., 2020; Esau, 1960), and we refer the reader to Appendix B (§B2.1) for additional details on that point.

There are however some interesting aspects that are worth mentioning here and - to the best of our knowledge - are still not reported in the literature. The first one is the fact that the ~7-8 µm width pith cavity lining (PCL) that delimitates the inner surface of the WS particularly stands out with brighter voxels. This higher density of matter in the PCL is not clearly documented in the literature. Additional confocal microscopy images suggest that the PCL is made of a densely packed fibrous structure, which could explain such a high mass density (Appendix B, §B.2). This structure would originate from the formation of the central cavity of the stem when parenchyma cells that form the pith collapse during the maturation of the plant (Kirby, January 2023 from https://www.fao.org/3/Y4011e/y4011e05.htm), thus accumulating cellulose-based material and other carbohydrates at this very position. The second striking feature is the mesh-like pattern that we discern on the surface of the PCL on the 3D images of Figs. 1a and 1b. It seems that this structural feature has never been explicitly described before, even if unannotated SEM images previously published suggest similar patterns with WS (Hansen et al., 2011). This pattern, with a mesh size of about the transverse size of a WS cell (~70 µm), is not associated with a rugosity of the inner surface of the wheat straw at the resolution of µCT: it is the presence of voxels with higher mass densities within the PCL that draw this pattern. It does not systematically match with the walls of the cells that are found immediately behind the PCL as is revealed by careful inspection of SEM images and tomographic slices (Appendix B, §B.3). Based on SEM experiments, we show that the mesh results from the presence of a dense, fibrous, mesh-like cellulosic structure within the PCL, that can be revealed when removing the thin external pellicle material that covers the PCL. Again, such a structure is certainly reminiscent of the complex mechanisms that take place during the plant growth, especially during the hollow stem formation, including the probable stacking and squeezing of the cells that eventually form the PCL.

Enzymatic degradation of WS as imaged by µCT

Our approach is an ex-situ approach where the enzymatic treated samples are dried before imaging. As mechanical damage and/or deformation potentially occurs when a same sample is submitted to successive cycles of enzymatic treatment/imaging, we use multiple native samples (see Methods for details). Each one is submitted to the enzymatic cocktail for a given duration and then imaged after drying. The cocktail is a commercial mixture of enzymes (Novozymes A/S) that have complementary activities for the saccharification of generic lignocellulosic substrates, combining enzymes actives on cellulose and on hemicelluloses (Marjamaa and Kruus, 2018) . The different durations of the enzymatic treatment are chosen according to the measurement of the cocktail activity using a chemical procedure detailed in Appendix C. In total, we have six different conditions: five being in a time range where the enzymatic action is clearly measurable and evolves continuously with time (30 min to 2 hours), and one 'limiting' case where the WS is exposed to the cocktail for 72 h (see Appendix B, §B.4 for details about the preparation of this sample). The analysis then consists in comparing the images obtained for the same sample before and after the enzymatic treatment.

Figs. 2-4 provide some significant results of this comparison, with images obtained after 30 min, 1 h, and 72 h of enzymatic treatment, respectively. The complete set of images for all the exposure times is given in Appendix B, §B.5.

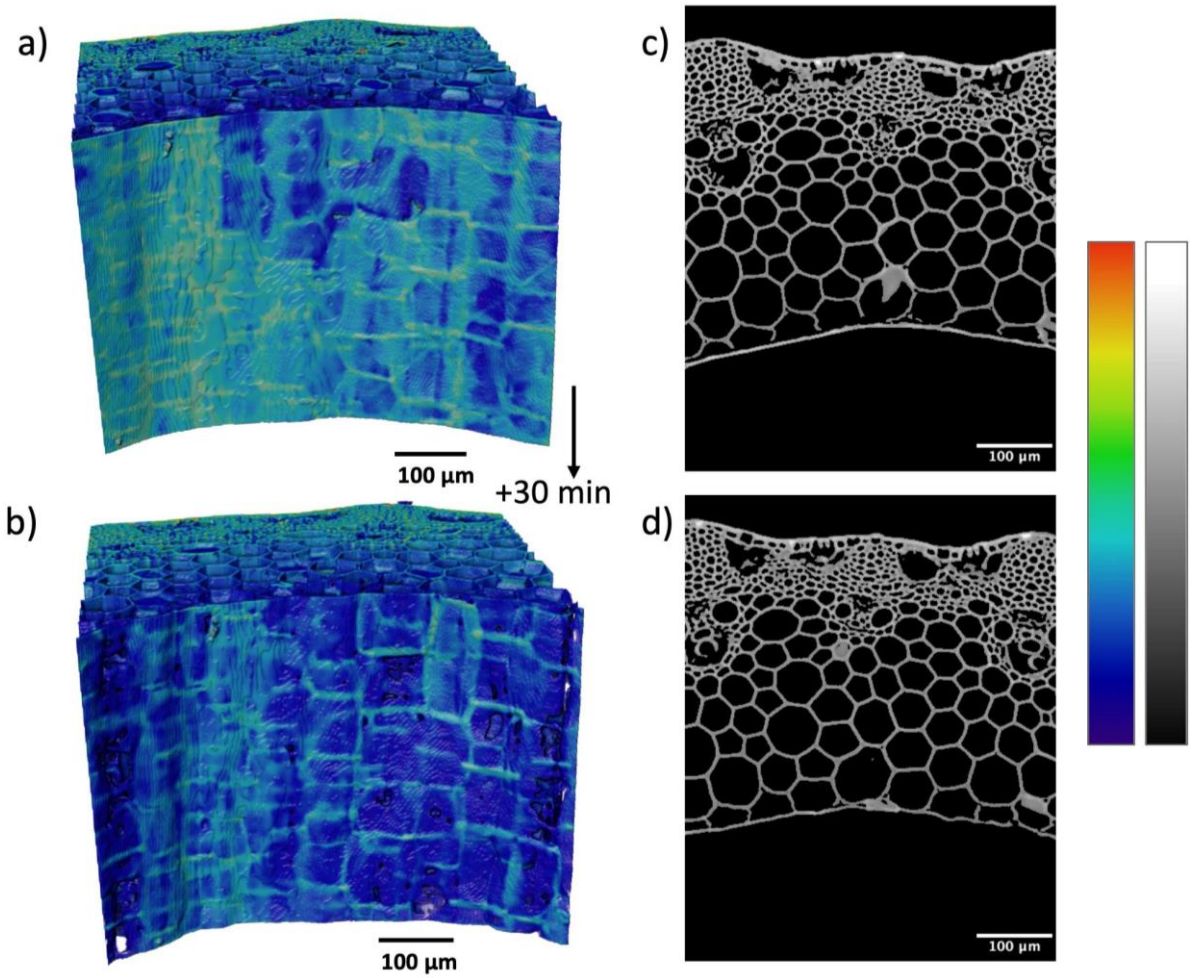

Fig. 2 µCT images of wheat straw before and after 30 min of enzymatic degradation. a) 3D volume rendering before treatment. b) 3D volume rendering after treatment at the same location of the sample. c) Tomographic transverse slice before treatment. d) Tomographic transverse slice after treatment at the same location of the sample. The top and bottom images come from different 3D scans but can be compared thanks to the histogram matching procedure detailed in Appendix A, §A.2.1. As a result, the colormap shown in the right is the same for the top and bottom images. The procedure for spatial adjustment of the native and digested images is given in Appendix A, §A.2.2.

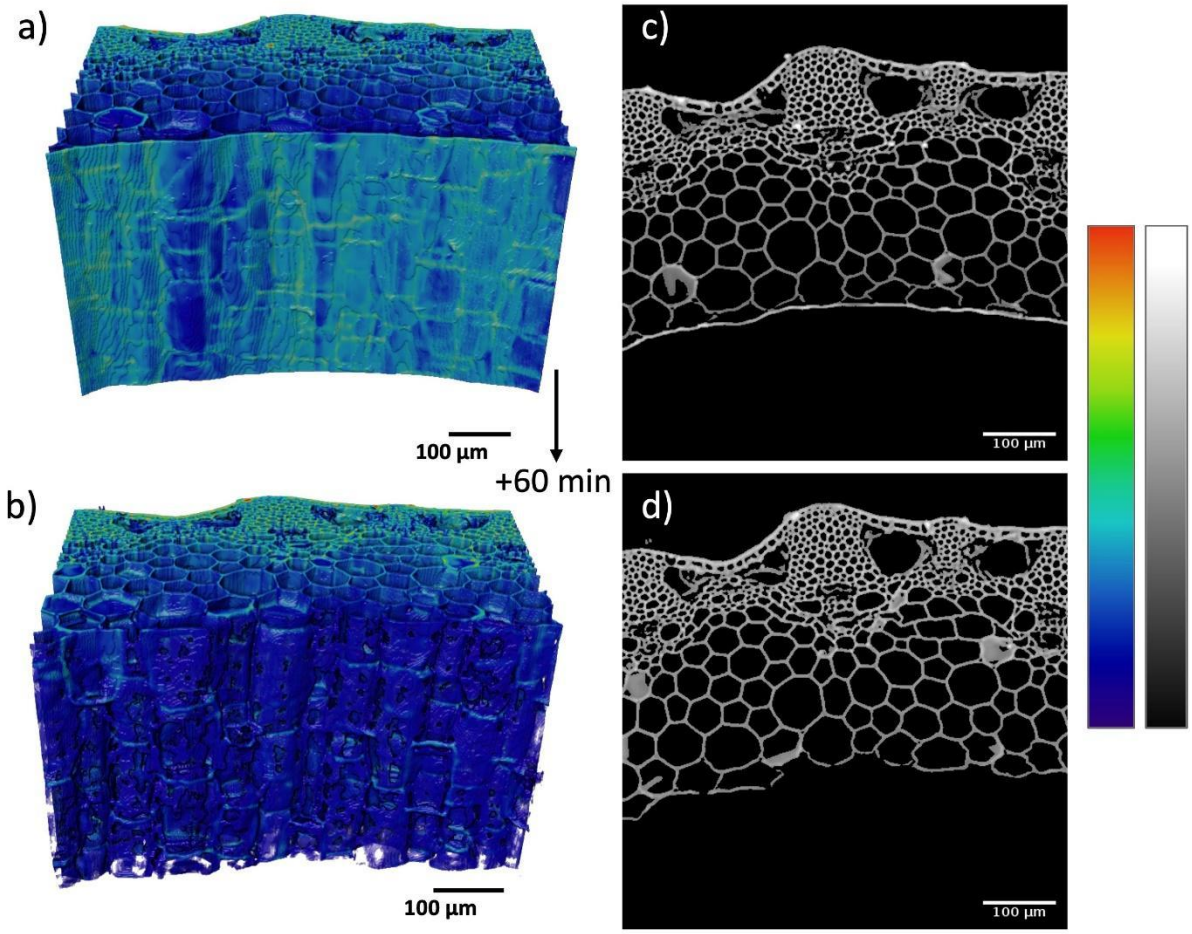

293

294 **Fig. 3 µCT images of wheat straw before and after 1 hour of enzymatic degradation.** a) 3D volume rendering
295 before treatment. b) 3D volume rendering after treatment at the same location of the sample. c) Tomographic
296 transverse slice before treatment. d) Tomographic transverse slice after treatment at the same location of the
297 sample.

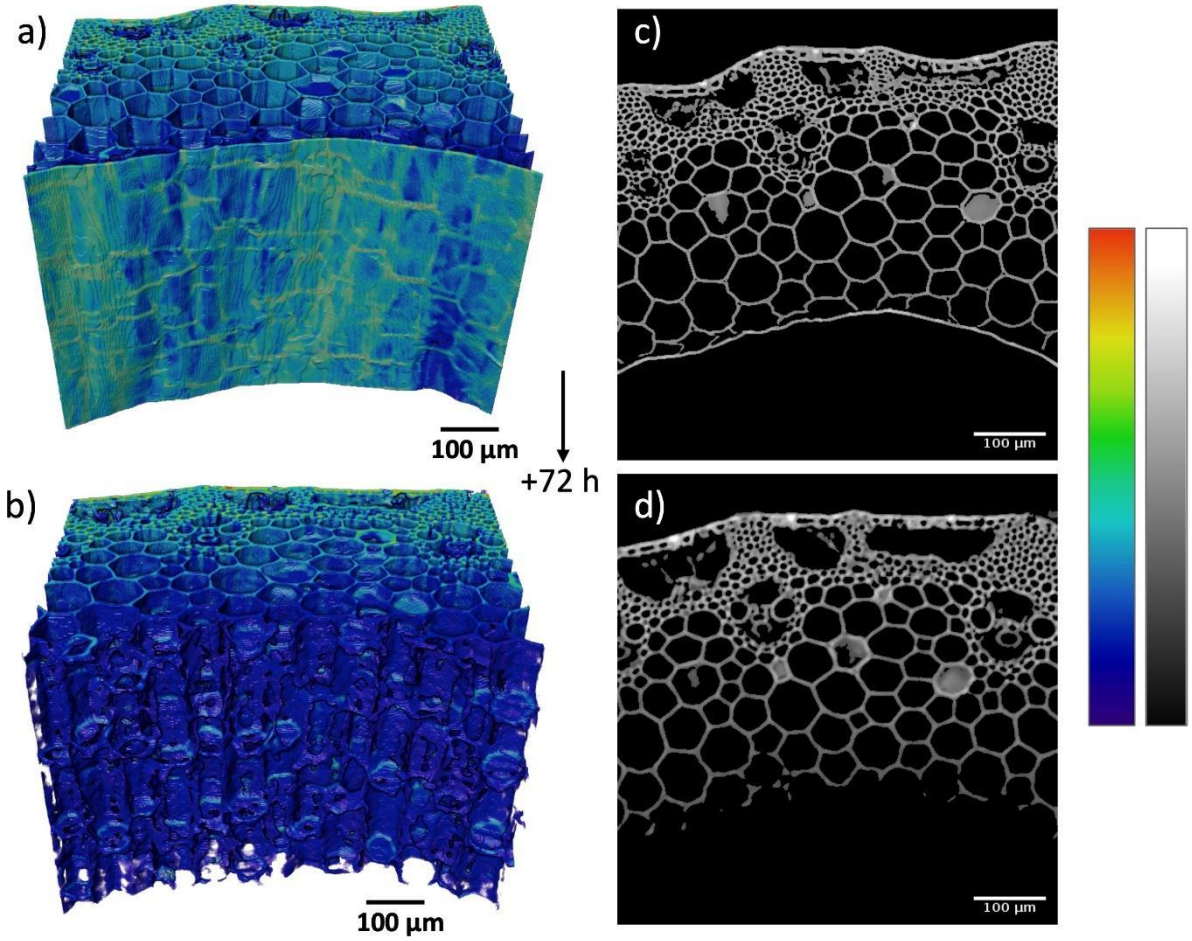

Fig. 4 µCT images of wheat straw before and after 72 hours of enzymatic degradation. a) 3D volume rendering before treatment. b) 3D volume rendering after treatment at the same location of the sample. c) Tomographic transverse slice before treatment. d) Tomographic transverse slice after treatment at the same location of the sample.

General features

A first qualitative and human-driven analysis of these images already gives an interesting picture of how the deconstruction occurs. After 30 min of enzymatic digestion (Fig. 2), one clearly observes a decrease in the average voxel intensity, i.e., grey level (GL) value, in the PCL for the digested wheat straw. On the tomographic slices (Figs. 2c and 2d), the PCL is still present after the enzymatic attack, but its GL values are now close to those of the internal cell walls. The corresponding volume rendering confirms this observation (Figs. 2a and 2b), with the PCL that appears blueish over the entire height of the sample after the enzymatic treatment. However, we still distinguish the mesh pattern of the PCL, showing that there remain some heterogeneities in mass density. At 1 h of degradation (Fig. 3), the decrease in GL at the PCL is even more marked. In some places, the PCL is not visible anymore, as clearly seen in Fig. 3d. This results in the appearance of some 'holes' in the inner structure of the WS, as shown in Fig. 3b. On the other hand, the initial mesh pattern of the PCL is still identifiable on this

picture, meaning that the denser parts of the PCL still resist to the attack at 1 h of degradation. Finally, at 72 h of degradation (Fig. 4), the PCL is totally digested, and the parenchyma cells originally located at the immediate vicinity of the PCL are also attacked. As those cells are now 'opened', this leads to an inner structure that appears hilly and rugged, with a roughness that corresponds to the size of the cells. In the meantime, no enzymatic degradation of the epidermis is evidenced. Overall, these naked-eye observations suggest that the enzymes of the cocktail attack the WS structure from its inner surface, first weaken and then dissolve the PCL, and finally progress into the inner WS structure and degrade it. Apart from that, the human eye is not capable of finding other obvious changes in the µCT images as the degradation occurs.

Quantitative markers of enzymatic degradation

For taking a step further in the analysis, a computer-driven examination of the µCT images is necessary. There are many possible ways to perform such an analysis. Here we focus on a 'coarse-grained' statistical approach aiming at giving a semi-quantitative evaluation of the enzymatic action. The approach consists in defining parallelepiped regions of interest (ROIs) in the samples, based on the changes observed with a naked eye. Three types of ROIs are defined in this way (see the inset in Fig. 5a for a schematic representation, full details of the procedure are given in Appendix A, §A.2.3). They correspond to (1) the outer epidermis part (blue), (2) the inner parenchyma part (green), (3) the PCL region (red), with ROI volumes of 1500, 25000 and 1500 μm^3, respectively. For statistical significance, 1000 ROIs are defined for a given sample, each ROI being randomly located along the sample height and circumference.

In Fig. 5a, we show the distributions of GLs for all the voxels within a given type of ROI, before and after enzymatic attack. As we are only interested in the mass distribution in the PCW material, the GL values are obtained by subtracting to the raw data the GL value chosen as a threshold to separate the PCW material from air (Appendix A, §A.2.4). The GLs are then divided into classes of equal sizes (200). For visibility, the distributions are not plotted as histograms but as curves where the *x*-axis values give the centre of each class, and the *y*-axis the number of voxels in each class.

Clearly, the distributions in the epidermis region of the sample (blue curves) are identical before and after the action of the enzymes. In other words, µCT does not measure any change in mass distribution at those locations in the sample. A similar conclusion can be drawn for the inner parenchyma for which the distributions are also similar before and after treatment (green curves). On the other hand, the results obtained for the PCL regions (red curves) show a strong shift of the distribution towards lower GL values after the enzymatic attack: the GL values in the range [2000-6000], representative of the bright voxels of the PCL in the native image (red crosses in Fig. 5a), are no longer present in the digested sample (red dots). Importantly, such an effect is not found for a control

sample that has experienced the same protocol of preparation than the sample of Fig. 5a but in absence of the enzymatic cocktail (Appendix A, §A.6). This confirms that the evolution of the GLs distribution observed for the PCL in Fig.5a (from red crosses to red points) is the signature of the hydrolysis that occurred in the PCL region, for a 90 min treatment in this very case. In Fig. 5b, we focus on the kinetics of this shift, with results obtained in the PCL regions for different durations of enzymatic treatment. The obtained distributions are clearly different from one to another, with a progressive deformation of the distributions towards lower GL values and a significant decrease in the number of PCW material voxels as deconstruction occurs.

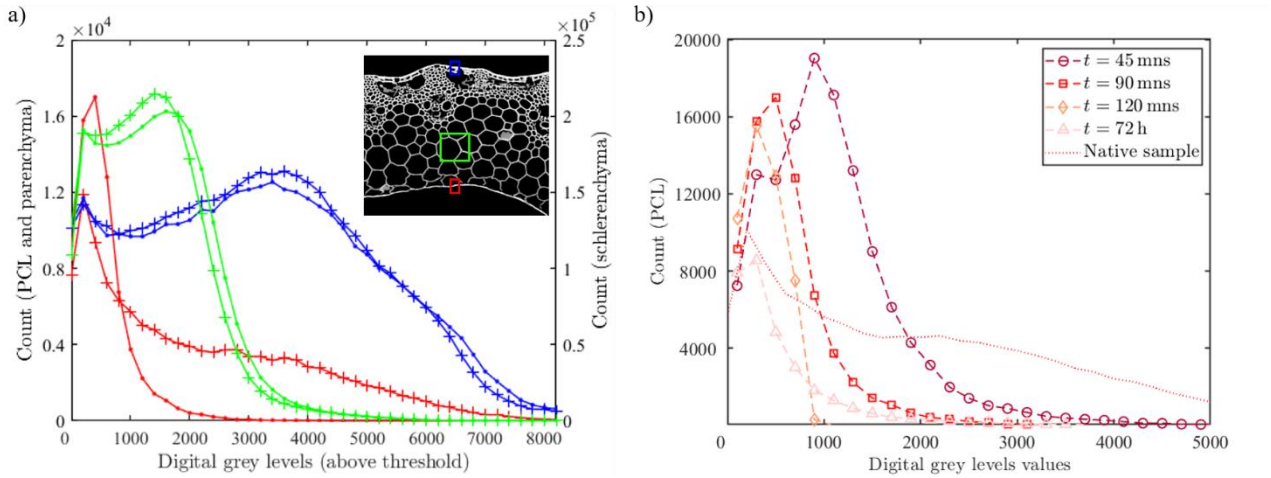

Fig. 5 Mass density distribution analysis a) Grey level distributions before (dots) and after enzymatic attack (crosses), for a 90 minutes long enzymatic attack. Each colour refers to a given type of ROI, as illustrated in the inset: across the PCL (red), 125 µm away from the PCL within the parenchyma (green), and across the epidermis (blue), see Appendix A, §A.2.3 for details. The left *y*-axis scale is for the PCL (red) and sclerenchyma ROIs (blue), while the right *y*-axis scale is for the larger parenchyma ROIs (green). b) Grey level distributions, within the ROIs located across the PCL (red in Figure 5a), for different duration of the enzymatic attack (see legend). A typical distribution for a native sample is also shown. The y-axis values are the absolute number of voxels in each class, meaning that the area below the curve is roughly equal to the total number of voxels belonging to the PCW material.

Generally speaking, two important informative quantities can be extracted from GL distributions such as those shown in Figure 5: (1) the total number of voxels in the ROIs, which gives a good estimate of the average volume of PCW material in the boxes, (2) the average GL value in these boxes. In Fig. 6, we provide the evolution of those two indicators as a function of time for all the samples investigated and for each type of ROI. Each indicator is normalized by its value before enzymatic degradation, to get rid of the natural variation between different WS samples.

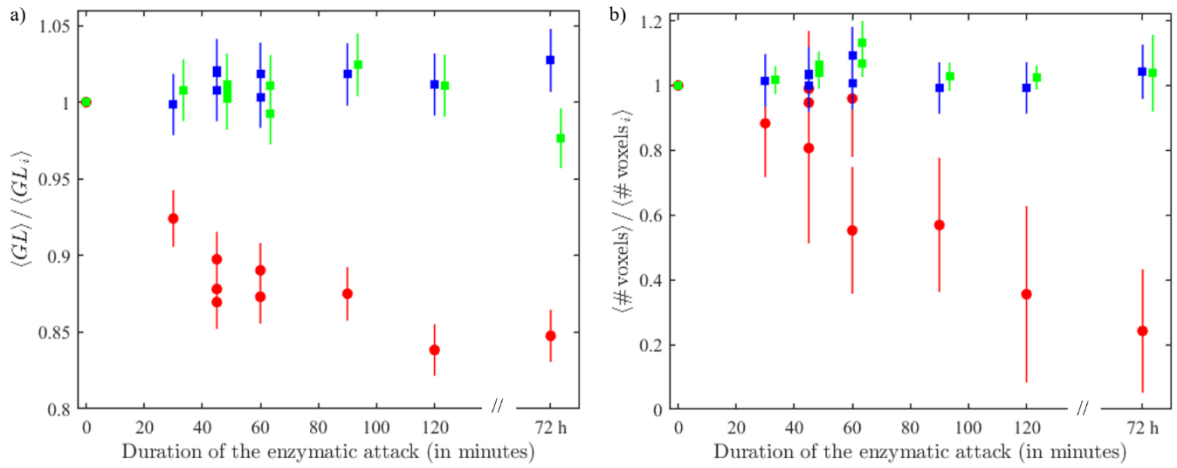

Fig. 6 Quantifying the enzymatic deconstruction as a function of time. a) Mean value of the grey levels for the voxels belonging to the PCW material, $< GL >$, b) total number of voxels belonging to the PCW material, $< \#\, voxels >$, as a function of the duration of enzymatic attack. The averaging is performed over 1000 ROIs. PCL ROIs: red data points, epidermis/parenchyma ROIs: respectively blue and green data points. The latter are slightly shifted along the x-axis for sake of clarity. For each sample, the data point are rescaled by the value measured on the native sample ($< GL_i >$ and $< \#\, voxels_i >$). The errors bars come from the uncertainty on the segmentation threshold (Appendix A, §A.2.4).

The results of Fig. 6 directly quantify the efficiency of the enzymatic attack and its kinetics and thus nicely complement the visual inspection of the raw CT images. The markers of Fig. 6a also embed the main findings of Fig. 5 regarding the PCL: the evolution of the GLs distribution resulting from the hydrolysis leads to a decrease of the mean value and of the number of voxels belonging to the PCW material. This is respectively associated with a shift of the GLs distribution towards lower GLs values and a decrease in the area below the distribution (see Fig. 5.a and 5.b). This is because initially bright voxels (high GLs) of the PCW material located in the PCL become fainter following the hydrolysis (their GLs decrease, as also observed in the 3D volume rendering of Fig. 2 to 4) and eventually disappear (this evolution and its physical interpretation are further discussed in the following). As the contrast between these voxels and the air background decreases, they are harder to detect on the 3D images against the air background. Consequently, the uncertainty associated with the choice of the segmentation threshold is higher than for the others ROIs considered (epidermis and parenchyma), as shown by the larger errors bars for the total number of PCW material at PCL in Figure 6.b (see Appendix A, §A.2.4). Two important conclusions regarding the underlying physics of the enzymatic degradation can be drawn at this stage:

. First, regarding the location of the enzymatic attack, the data of Fig. 6 confirm that the enzymatic degradation essentially proceeds from the PCL, as observed qualitatively on the images. The markers of the degradation do not exhibit any significant evolution in the epidermis and parenchyma (Fig. 6a and 6b). Only the PCL is affected by the enzymes both in terms of voxel numbers (total volume) and average intensity (density). However, we know that the parenchyma cells at the immediate vicinity of

406 the PCL start to be degraded after 1 h of enzymatic treatment (Fig. 4 and S2.5). This is not visible in Fig.
407 6 as those cells do not belong to the parenchyma ROIs that we defined 125 µm away from the PCL. All
408 these findings are in accordance with the results of the literature. For instance, Bertrand *et al.* analysed
409 the decomposition of WS in soil based on biochemical features and histology (Bertrand et al., 2006).
410 As in the present work, only the PCL and parenchyma cells disappear after exposing raw samples to
411 soil microorganisms for 119 days. A similar effect was observed after 8 weeks of composting by
412 Dresbøll *et al.* (2006). In addition, Hansen *et al.* (2013)confirmed that enzymes from commercial
413 cocktails adhere mostly to the PCL and parenchyma cells, making them the most important factor
414 determining WS digestibility. In our case, the rather short durations of enzymatic treatment as
415 compared to the cited studies makes it possible to observe that the PCL is quickly and strongly attacked
416 in the first place, while the parenchyma degrades much more slowly with time. Besides the fact the
417 PCL is obviously the first material that the enzymes encounter during the attack, it therefore seems
418 very likely that the parenchyma material itself if more resistant to the enzyme action than the PCL.
419 This in turn would be due to some - still not so well documented - differences in the structure and
420 chemical composition of both materials. The presence and/or arrangement of lignin in the PCL and
421 parenchyma cell walls is probably one explanation. Lignin, a complex heterogeneous alkyl-aromatic
422 polymer, is embedded in the cellulose/hemicellulose matrix of the plant cell walls, and is indeed known
423 to play a crucial role in the recalcitrance of plants to enzymatic deconstruction (Kim K. H. and Kim C. S.
424 2018). Regarding the epidermis, the absence of observable degradation is due to the high recalcitrance
425 of this anatomical feature, notably due to layers of cutin which is the main component of the
426 epidermis, also named cuticle. This high molecular weight biopolyester is known to embed wax and
427 fats, forming a shield that protects the epidermis from external aggressions as enzymatic attacks
428 (Hansen et al., 2013).

429 . Second, regarding the way the enzymatic attack proceeds at the PCL, the following observations can
430 be made. At the voxel scale, the GL is related to the effective mass density of the PCW material.
431 Therefore, a decrease in the voxel GL can have two different origins: (i) a loss in material (i.e. cellulose
432 and/or hemicellulose), (ii) a local swelling of the microstructure without any loss of material. As
433 evidenced in the images of Figs. 3-4, and quantified in Fig. 6b, the PCL clearly loses some material at
434 time > 60 min and eventually disappears. However, at shorter times (< 60 min), it is possible that the
435 stacked microfibril structure of the cellulose in the PCL (Appendix B, §B.2) may disorganize and then
436 swells under the enzymatic action, occupying a larger space, and thus leading to a less dense -and thus
437 less attenuating- equivalent material at the voxel resolution. This would explain why the average GL of
438 the PCL (Fig. 6a) seems to decrease faster than the number of voxels in the corresponding ROIs (Fig.
439 6b). The evolution of the GLs distribution shown in Fig. 5 would then result from a combination of

these two mechanisms: bright pixels that become attenuated induce a shift of the distributions towards lower values, while the loss of material induces a decrease in the number of PCW voxels (decrease of the area below the distribution).

The data of Fig. 6b are too noisy to strictly conclude on that point, essentially because of the spatial resolution of the present µCT images is still not sufficient. However, it seems reasonable to hypothesize that the swelling of the PCL is the first step of the enzymatic degradation, or at least plays an important role at the very beginning of the enzymatic attack. The commercial cocktail used in our study contains hemicellulases, but also a mixture of cellulases (probably endoglucanases (EG), cellobiohydrolases (CBH) and glucosidases), but the precise composition is not provided. EG and CBH are known to penetrate cellulose fibres and pry apart the microfibrils, thus disrupting the fibres surface (Lee et al., 2000). Also, several non-catalytic proteins - that may also compose the commercial cocktail that we used - are involved in changes in the cellulose microfibril structure, such as peeling and disorganization, thus favouring cellulose deconstruction (Arantes and Saddler, 2010).

A focus on the 3D heterogeneity of the enzymatic attack

We now go beyond the average, statistical analysis of the µCT images that we just presented and focus on the structural changes occurring at the PCL at the local scale. To that end, we produce 2D images by 'unrolling' the PCL after paving it with neighbouring parallelepiped-shaped boxes (Appendix A, §A.2.5). A spatial adjustment procedure allows to position the 2D images obtained before and after digestion in the same spatial reference frame (Appendix A, §A.2.2). As we focus on the PCL, this analysis can be performed only if the PCL is not heavily deconstructed, e.g., with missing cellular walls. It is therefore restricted to short durations of exposure to the enzymatic cocktail (≤ 45 min).

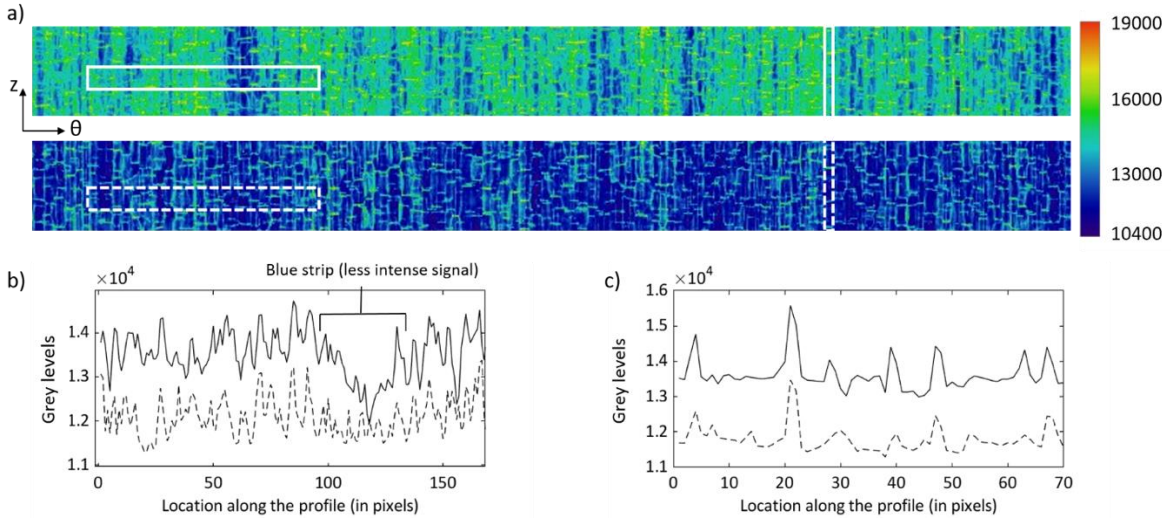

Fig. 7 PCL degradation at local scale a) 2D visualizations of the internal surface of a sample before (top) and after (bottom) 45 min of enzymatic attack. The correspondence between the grey levels and the colormap is shown on the right. b) Grey level profiles along the leftmost box, averaged over the box height: native sample (solid line) and digested sample (dashed line). c) Grey level profile along the rightmost box, averaged over the box width: native sample (solid line) and digested sample (dashed line).

Figure 7a,top is the 2D visualization of the PCL of a native wheat straw, while its digested counterpart is in Figure 7a,bottom. Heterogeneities in mass density can be seen at several scales. At large scale, some darker strips that are roughly aligned with the sample longitudinal axis, and sometimes with varying width, are discernible. A GL profile along the θ direction (leftmost white box) is shown as a solid line in Figure 7b and gives an example of such a large-scale heterogeneity (blue strip position). At smaller scale, the mesh-like network of brighter voxels that we already discussed (see also Appendix B, §B.3) is clearly visible on the images. A profile along the *z* direction of the rightmost white box displays peaks that correspond to this pattern (solid line in Figure 7c). The main effect observed in the digested image (Figure 7a,bottom) and the profiles extracted from this image (dashed lines in Figure 7b,c) is a global lowering of the GL values. A more careful inspection reveals that the large scale heterogeneities are attenuated after digestion, with a 'smoothing' of the profile in Fig. 7b as if the darker regions were less affected by the enzymatic attack. Another striking feature is that the mesh pattern still remains discernible on the digested sample, but with lower GL values.

Fig. 7 notably shows that, despite the effect of a 45 min enzymatic treatment, some spatial correlation remains between the 2D images of the PCL before and after the attack. In other words, some of the original heterogeneities in mass density in the PCL appear to be conserved after the attack. We can investigate this more precisely by analysing the change in the GL values as a function of the initial mass density at different positions in the PCL. This is done by dividing the GL distribution in several bins, and then comparing the native ($\langle GL_i \rangle$) and final ($\langle GL \rangle$) GL values averaged over the PCL voxels that initially belongs to each bin. In Fig. 8a, we plot the ratio $\langle GL \rangle / \langle GL_i \rangle$ as a function of $\langle GL_i \rangle$ for two enzymatic treatments, i.e., 30 and 45 min (respectively black and red data points). While in Fig. 6a we were looking at the evolution of $\langle GL \rangle / \langle GL_i \rangle$ over all the PCW material, here we are investigating the evolution of this parameter at the local scale, based on the initial mass density at distinct regions in the PCL, e.g., the dense mesh-like structure vs the less dense regions (for instance those responsible for the large scale heterogeneities of Fig. 7a,top). In Fig. 8a, the values of the ratio obtained after a random re-ordering of the voxels of the final images are also shown (dashed lines). The observed deviations from the random case indicate a positive correlation between the highest, respectively lowest, GLs on the initial and on the final images. The correlation is clearly marked at 30 min. At 45 min, the differences are only significant for the highest and lowest $\langle GL_i \rangle$ and the data clearly tend

towards the random case. This suggests a loss of correlation over a large part of the sample, which corresponds to the disappearance of most of the distinctive structural features of the PCL.

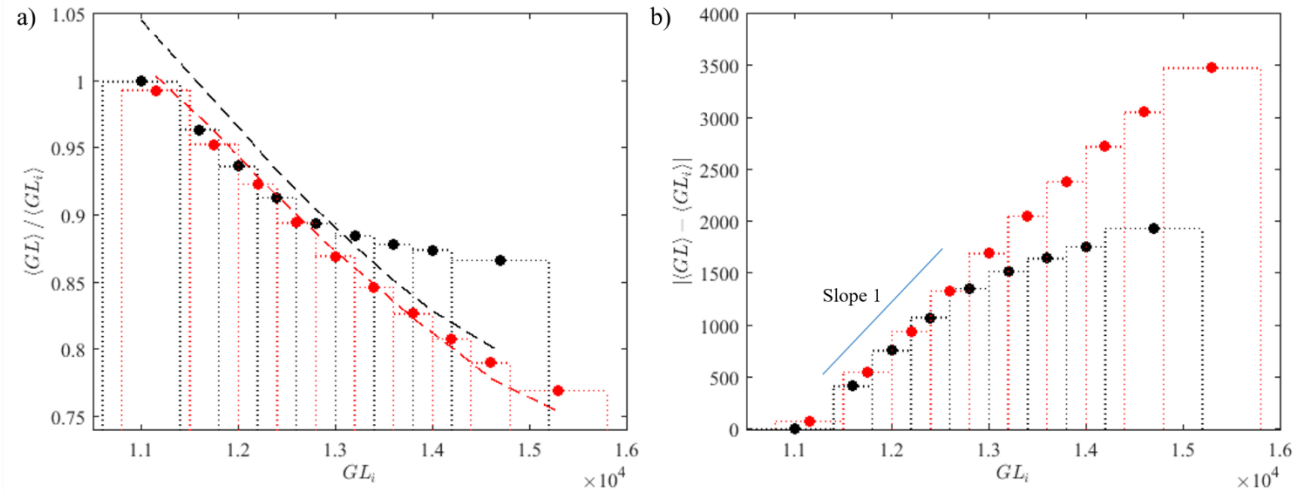

Fig. 8 Analysis of the enzymatic attack heterogeneity a) Ratio of the GL values after and before enzymatic attack, $< GL >/< GL_i >$, as a function of the GLs of the native sample. b) Absolute value of the difference between the GL values after and before enzymatic attack, $|< GL > - < GL_i >|$ as a function of the GLs of the native sample. Each data point is obtained by averaging over all the voxels whose initial GL value belongs to the corresponding bin, highlighted by the vertical dotted lines. The dashed lines show the result obtained with a random re-ordering of the image obtained after enzymatic attack. Black, respectively red, lines and data points are for a 30 min, respectively 45 min, duration of enzymatic attack.

Another way of looking at these results is to plot the absolute value of the difference between the initial and final GL values, $|\langle GL \rangle - \langle GL_i \rangle|$, as a function of $\langle GL_i \rangle$. This representation provides a more direct view of the process as it gives the actual loss in mass density in the PCL during the enzymatic attack. One first important observation is that the PCL regions that are initially the less dense (~11000 in GL) do not show any loss in mass density as compared to the initial state. This strongly suggests that the enzymes do not have any activity on those "loose" PCL regions - in the period of time investigated. The reason for that resistance is less obvious but most probably relies on the fact that the substrate of the enzymes is absent or is not accessible at these very locations. At higher initial GL values (11000-13000), the enzymatic action becomes visible with a loss in mass density that increases linearly with $\langle GL_i \rangle$. It is then clear that the enzymes can work on those denser PCL regions. In addition, the slope of this linear increase is very close to 1, thus suggesting that the enzymes degrade the PCL until its structure and composition resemble those of the "loose" regions that we just discussed, at GL $\approx$ 11000. Furthermore, the loss in density is the same at 30 and 45 min of enzymatic treatment, which indicates that 30 min (or less) is enough to reach that state. At higher initial GL values (> 13000), the loss in mass density still increases linearly with the initial density in the PCL after a 45 min attack. On the other hand, the enzymatic digestion of those regions is clearly not complete at 30 min, with losses in mass

density that are still lower than at 45 min. For clarity, we recall that Fig. 8 and the associated results are from data obtained before the PCL starts to disappear from the μCT images (t < 45 min) - since a similar local-scale analysis becomes too complicated and risky at higher times. Consequently, the conclusions that we draw are only for that period time, but still suggest that the PCL is attacked by the enzymes until it reaches a given state with a GL value of ~11000. After 45 minutes, the deconstruction mechanism is probably different from a "simple" swelling or loss of material from the structure, with the possible detachment of small pieces of PCL for instance.

4. Conclusion

The results of this paper highlight the relevance of X-ray microtomography as a tool to study the enzymatic deconstruction of a typical lignocellulosic biomass, wheat straw. This imaging technique is particularly well-suited to reveal the modification of the plant cell walls within the sample, at different stages of the enzymatic deconstruction, while considering sample heterogeneities in terms of structure and composition at different length scales. In the present case, working with a raw wheat straw sample, enzymatic hydrolysis is shown to proceed progressively from the PCL while the epidermis remains unaffected (at the spatial resolution of the μCT technique). Markers of the degradation are extracted from a thorough 3D image analysis and can be used to track the kinetics of the hydrolysis. Also, 3D images obtained for a given sample are compared at a local scale, before and after degradation, revealing the heterogeneity of the enzymatic attack, depending on the location on the PCL, a highly heterogeneous anatomical feature, in terms of material density.

We believe that this work is a first step in the use of μCT for understanding the action of enzymes on a real substrate and in real-life conditions. In addition, the analysis that we perform - based on tools and concepts purposely developed for this study - can clearly serve as a μCT generic workflow for many further works in the field, like studying the action of one or several specific enzyme(s) rather than enzymatic cocktails, and/or the degradation of other types of biomass structures.

Acknowledgments

We thank Alain Jauneau and Cécile Pouzet for technical assistance on confocal imaging at the TRI-FR AIB imaging platform facility (FR 3450 CNRS-UT3, Castanet-Tolosan, France). We also thank Bruno Payre from the Centre de Microscopie Électronique Appliquée à la Biologie (CMEAB) of the Université Paul Sabatier at Toulouse, France. The research federation FERMAT (Université de Toulouse, CNRS, Toulouse France) is acknowledged for providing access to its X-ray tomography facility.

Appendixes A, B and C. Supplementary data

Supplementary data to this article can be found online at https://doi.org/xxx

Funding

This work was partially supported by an internal grant from the French National Research Institute for Agriculture, Food and Environment (INRAE), project Splendid.

Author contributions

PD and CYM conceived and designed the experiments. SB and PD performed the experiments. SB, AB, CYM and PD analysed the data. All authors discussed the results and contributed to paper writing.

Competing interests

The authors declare no competing interests.

Data availability

The data supporting the findings of this study are reported in the main text or the Appendix. Raw data can be obtained from the corresponding authors upon reasonable request.

References

Amos, R.A., Mohnen, D., 2019. Critical Review of Plant Cell Wall Matrix Polysaccharide Glycosyltransferase Activities Verified by Heterologous Protein Expression. Frontiers in Plant Science 10.

Arantes, V., Saddler, J.N., 2010. Access to cellulose limits the efficiency of enzymatic hydrolysis: the role of amorphogenesis. Biotechnology for Biofuels 3, 4. https://doi.org/10.1186/1754-6834-3-4

Badruna, L., Burlat, V., Roblin, P., Enjalbert, T., Lippens, G., Venditto, I., O'Donohue, M.J., Montanier, C.Y., 2021. The Jo-In protein welding system is a relevant tool to create CBM-containing plant cell wall degrading enzymes. New Biotechnology 65, 31–41. https://doi.org/10.1016/j.nbt.2021.07.004

Bertrand, I., Chabbert, B., Kurek, B., Recous, S., 2006. Can the Biochemical Features and Histology of Wheat Residues Explain their Decomposition in Soil? Plant Soil 281, 291–307. https://doi.org/10.1007/s11104-005-4628-7

Botany of the wheat plant - E.J.M. Kirby [WWW Document], n.d. URL https://www.fao.org/3/Y4011e/y4011e05.htm (accessed 9.5.22).

Brereton, N.J.B., Ahmed, F., Sykes, D., Ray, M.J., Shield, I., Karp, A., Murphy, R.J., 2015. X-ray micro-computed tomography in willow reveals tissue patterning of reaction wood and delay in programmed cell death. BMC Plant Biol 15, 83. https://doi.org/10.1186/s12870-015-0438-0

598 Cherubini, F., 2010. The biorefinery concept: Using biomass instead of oil for producing energy and
599 chemicals. Energy Conversion and Management 51, 1412–1421.
600 https://doi.org/10.1016/j.enconman.2010.01.015

601 Derome, D., Griffa, M., Koebel, M., Carmeliet, J., 2011. Hysteretic swelling of wood at cellular scale
602 probed by phase-contrast X-ray tomography. Journal of Structural Biology 173, 180–190.
603 https://doi.org/10.1016/j.jsb.2010.08.011

604 Devaux, M.-F., Jamme, F., André, W., Bouchet, B., Alvarado, C., Durand, S., Robert, P., Saulnier, L.,
605 Bonnin, E., Guillon, F., 2018. Synchrotron Time-Lapse Imaging of Lignocellulosic Biomass Hydrolysis:
606 Tracking Enzyme Localization by Protein Autofluorescence and Biochemical Modification of Cell Walls
607 by Microfluidic Infrared Microspectroscopy. Frontiers in Plant Science 9.

608 Dresbøll, D.B., Magid, J., 2006. Structural changes of plant residues during decomposition in a compost
609 environment. Bioresource Technology 97, 973–981. https://doi.org/10.1016/j.biortech.2005.05.003

610 Gilbert, H.J., 2010. The Biochemistry and Structural Biology of Plant Cell Wall Deconstruction. Plant
611 Physiology 153, 444–455. https://doi.org/10.1104/pp.110.156646

612 Gilmore, S.P., Lillington, S.P., Haitjema, C.H., de Groot, R., O'Malley, M.A., 2020. Designing chimeric
613 enzymes inspired by fungal cellulosomes. Synthetic and Systems Biotechnology 5, 23–32.
614 https://doi.org/10.1016/j.synbio.2020.01.003

615 Hansen, M.A., Hidayat, B.J., Mogensen, K.K., Jeppesen, M.D., Jørgensen, B., Johansen, K.S., Thygesen,
616 L.G., 2013. Enzyme affinity to cell types in wheat straw (Triticum aestivum L.) before and after
617 hydrothermal pretreatment. Biotechnology for Biofuels 6, 54. https://doi.org/10.1186/1754-6834-6-
618 54

619 Hansen, M.A.T., Kristensen, J.B., Felby, C., Jørgensen, H., 2011. Pretreatment and enzymatic hydrolysis
620 of wheat straw (Triticum aestivum L.) – The impact of lignin relocation and plant tissues on enzymatic
621 accessibility. Bioresource Technology 102, 2804–2811.
622 https://doi.org/10.1016/j.biortech.2010.10.030

623 Hervé, C., Rogowski, A., Gilbert, H.J., Paul Knox, J., 2009. Enzymatic treatments reveal differential
624 capacities for xylan recognition and degradation in primary and secondary plant cell walls. The Plant
625 Journal 58, 413–422. https://doi.org/10.1111/j.1365-313X.2009.03785.x

626 Jones, D.H., Atkinson, B.S., Ware, A., Sturrock, C.J., Bishopp, A., Wells, D.M., 2021. Preparation,
627 Scanning and Analysis of Duckweed Using X-Ray Computed Microtomography. Frontiers in Plant
628 Science 11.

629 Kim, K.H., Kim, C.S., 2018. Recent Efforts to Prevent Undesirable Reactions From Fractionation to
630 Depolymerization of Lignin: Toward Maximizing the Value From Lignin. Frontiers in Energy Research 6.

631 Lee, I., Evans, B.R., Woodward, J., 2000. The mechanism of cellulase action on cotton fibers: evidence
632 from atomic force microscopy. Ultramicroscopy 82, 213–221. https://doi.org/10.1016/S0304-
633 3991(99)00158-8

634 Liberato, M.V., Silveira, R.L., Prates, É.T., de Araujo, E.A., Pellegrini, V.O.A., Camilo, C.M., Kadowaki,
635 M.A., Neto, M. de O., Popov, A., Skaf, M.S., Polikarpov, I., 2016. Molecular characterization of a family
636 5 glycoside hydrolase suggests an induced-fit enzymatic mechanism. Sci Rep 6, 23473.
637 https://doi.org/10.1038/srep23473

638 Liu, Q., Luo, L., Zheng, L., 2018. Lignins: Biosynthesis and Biological Functions in Plants. International
639 Journal of Molecular Sciences 19, 335. https://doi.org/10.3390/ijms19020335

Lopes, A. m., Ferreira Filho, E. x., Moreira, L. r. s., 2018. An update on enzymatic cocktails for lignocellulose breakdown. Journal of Applied Microbiology 125, 632–645. https://doi.org/10.1111/jam.13923

Marjamaa, K., Kruus, K., 2018. Enzyme biotechnology in degradation and modification of plant cell wall polymers. Physiologia Plantarum 164, 106–118. https://doi.org/10.1111/ppl.12800

Mathers, A.W., Hepworth, C., Baillie, A.L., Sloan, J., Jones, H., Lundgren, M., Fleming, A.J., Mooney, S.J., Sturrock, C.J., 2018. Investigating the microstructure of plant leaves in 3D with lab-based X-ray computed tomography. Plant Methods 14, 99. https://doi.org/10.1186/s13007-018-0367-7

Matsushima, U., Graf, W., Zabler, S., Manke, I., Dawson, M., Choinka, G., Hilger, A., Herppich, W.B., 2013. 3D-analysis of plant microstructures: advantages and limitations of synchrotron X-ray microtomography. International Agrophysics 27.

Mayo, S.C., Chen, F., Evans, R., 2010. Micron-scale 3D imaging of wood and plant microstructure using high-resolution X-ray phase-contrast microtomography. Journal of Structural Biology 171, 182–188. https://doi.org/10.1016/j.jsb.2010.04.001

Montanier, C., van Bueren, A.L., Dumon, C., Flint, J.E., Correia, M.A., Prates, J.A., Firbank, S.J., Lewis, R.J., Grondin, G.G., Ghinet, M.G., Gloster, T.M., Herve, C., Knox, J.P., Talbot, B.G., Turkenburg, J.P., Kerovuo, J., Brzezinski, R., Fontes, C.M.G.A., Davies, G.J., Boraston, A.B., Gilbert, H.J., 2009. Evidence that family 35 carbohydrate binding modules display conserved specificity but divergent function. Proceedings of the National Academy of Sciences 106, 3065–3070. https://doi.org/10.1073/pnas.0808972106

Morris, J.L., Puttick, M.N., Clark, J.W., Edwards, D., Kenrick, P., Pressel, S., Wellman, C.H., Yang, Z., Schneider, H., Donoghue, P.C.J., 2018. The timescale of early land plant evolution. Proceedings of the National Academy of Sciences 115, E2274–E2283. https://doi.org/10.1073/pnas.1719588115

Nassar, R.M.A., Kamel, H.A., Ghoniem, A.E., Alarcón, J.J., Sekara, A., Ulrichs, C., Abdelhamid, M.T., 2020. Physiological and Anatomical Mechanisms in Wheat to Cope with Salt Stress Induced by Seawater. Plants 9, 237. https://doi.org/10.3390/plants9020237

Novy, V., Aïssa, K., Nielsen, F., Straus, S.K., Ciesielski, P., Hunt, C.G., Saddler, J., 2019. Quantifying cellulose accessibility during enzyme-mediated deconstruction using 2 fluorescence-tagged carbohydrate-binding modules. Proceedings of the National Academy of Sciences 116, 22545–22551. https://doi.org/10.1073/pnas.1912354116

Strullu-Derrien, C., Kenrick, P., Tafforeau, P., Cochard, H., Bonnemain, J.-L., Le Hérissé, A., Lardeux, H., Badel, E., 2014. The earliest wood and its hydraulic properties documented in c. 407-million-year-old fossils using synchrotron microtomography. Botanical Journal of the Linnean Society 175, 423–437. https://doi.org/10.1111/boj.12175

Suuronen, J.-P., Peura, M., Fagerstedt, K., Serimaa, R., 2013. Visualizing water-filled versus embolized status of xylem conduits by desktop x-ray microtomography. Plant Methods 9, 11. https://doi.org/10.1186/1746-4811-9-11

Torres-Ruiz, J.M., Cochard, H., Mencuccini, M., Delzon, S., Badel, E., 2016. Direct observation and modelling of embolism spread between xylem conduits: a case study in Scots pine. Plant, Cell & Environment 39, 2774–2785. https://doi.org/10.1111/pce.12840

Trtik, P., Dual, J., Keunecke, D., Mannes, D., Niemz, P., Stähli, P., Kaestner, A., Groso, A., Stampanoni, M., 2007. 3D imaging of microstructure of spruce wood. Journal of Structural Biology 159, 46–55. https://doi.org/10.1016/j.jsb.2007.02.003

683 Vanholme, R., Demedts, B., Morreel, K., Ralph, J., Boerjan, W., 2010. Lignin Biosynthesis and Structure.
684 Plant Physiology 153, 895–905. https://doi.org/10.1104/pp.110.155119

685 Withers, P.J., 2007. X-ray nanotomography. Materials Today 10, 26–34.
686 https://doi.org/10.1016/S1369-7021(07)70305-X

687 Yancy-Caballero, D., Ling, L.Y., Archilha, N.L., Ferreira, J.E., Driemeier, C., 2017. Mineral Particles in
688 Sugar Cane Bagasse: Localization and Morphometry Using Microtomography Analysis. Energy Fuels 31,
689 12288–12296. https://doi.org/10.1021/acs.energyfuels.7b02247

690 Zeng, Y., Yarbrough, J.M., Mittal, A., Tucker, M.P., Vinzant, T.B., Decker, S.R., Himmel, M.E., 2016. In
691 situ label-free imaging of hemicellulose in plant cell walls using stimulated Raman scattering
692 microscopy. Biotechnology for Biofuels 9, 256. https://doi.org/10.1186/s13068-016-0669-9

693 Zhang, B., Gao, Y., Zhang, L., Zhou, Y., 2021. The plant cell wall: Biosynthesis, construction, and
694 functions. Journal of Integrative Plant Biology 63, 251–272. https://doi.org/10.1111/jipb.13055